AIP | Journal of Applied Physics

Theoretical insights on the electro-thermal transport properties of monolayer MoS2 with line defects

Dipankar Saha and Santanu Mahapatra

Citation: Journal of Applied Physics **119**, 134304 (2016); doi: 10.1063/1.4945582
View online: http://dx.doi.org/10.1063/1.4945582
View Table of Contents: http://scitation.aip.org/content/aip/journal/jap/119/13?ver=pdfcov
Published by the AIP Publishing

Theoretical insights on the electro-thermal transport properties of monolayer MoS_2 with line defects

Dipankar Saha[a] and Santanu Mahapatra[b]
Nano-Scale Device Research Laboratory, Department of Electronic Systems Engineering, Indian Institute of Science, Bangalore 560012, India

(Received 3 December 2015; accepted 25 March 2016; published online 6 April 2016)

Two dimensional (2D) materials demonstrate several novel electrical, mechanical, and thermal properties which are quite distinctive to those of their bulk form. Among many others, one important potential application of the 2D material is its use in the field of energy harvesting. Owing to that, here we present a detailed study on electrical as well as thermal transport of monolayer MoS_2, in quasi ballistic regime. Besides the perfect monolayer in its pristine form, we also consider various line defects which have been experimentally observed in mechanically exfoliated MoS_2 samples. For calculating various parameters related to the electrical transmission, we employ the non-equilibrium Green's function-density functional theory combination. However, to obtain the phonon transmission, we take help of the parametrized Stillinger-Weber potential which can accurately delineate the inter-atomic interactions for the monolayer MoS_2. Due to the presence of line defects, we observed significant reductions in both the charge carrier and the phonon transmissions through a monolayer MoS_2 flake. Moreover, we also report a comparative analysis showing the temperature dependency of the thermoelectric figure of merit values, as obtained for the perfect as well as the other defective 2D samples. © *2016 AIP Publishing LLC*.
[http://dx.doi.org/10.1063/1.4945582]

I. INTRODUCTION

The recent exploration of two dimensional (2D) layered materials as the potential candidates for alternative channels in nano-transistors and devices has spurred an enormous research interest.[1–7] These materials being all-surface in nature can exhibit superior electrical, optical, and mechanical properties such as better electro-statics, increased photo luminescence, and higher mechanical flexibility.[1,3,8] Apart from those properties, heat transport is also quite unique in such 2D materials.[9] For example, the unsuspended layer of graphene (with a carrier density of $\simeq 5 \times 10^{12}\,cm^{-2}$) can yield a very high value of mobility ($\sim 25\,000\,cm^2\,V^{-1}\,s^{-1}$ as reported in Ref. 10) along with a significantly high room temperature (RT)-thermal conductivity (around $600\,W\,m^{-1}\,K^{-1}$, while on-substrate).[9,11] For free-standing bilayer graphene, the carrier density could be even higher (in the order of $\sim 10^{14}\,cm^{-2}$), if we consider the "K" or the "Li" intercalants.[12,13] However, it is a well-known fact[14] that graphene has almost a near zero bandgap in its pristine form. On the contrary, monolayer of MoS_2 (one of the most stable transition-metal dichalcogenides (TMDs)), which is generally semiconducting in nature, shows a direct bandgap of $\sim 1.8\,eV$ for monolayer.[1,3] Besides, for monolayer MoS_2, the in-plane stiffness has been reported as $180 \pm 60\,N\,m^{-1}$ which is very much comparable with that of the steel.[8] Despite all these advantages, the intrinsic mobility and the RT-thermal conductivity in monolayer MoS_2 are the two major concerns.[1,15–17] As reported in Ref. 15, the measured thermal conductivity of monolayer MoS_2 is $34.5 \pm 4\,W\,m^{-1}\,K^{-1}$ at RT (which is significantly lower than that of single layer graphene).

However, such a low value of thermal conductivity can play a very significant role in tuning thermoelectric (TE) figure of merit (FOM) to any higher value. Perhaps that is a quite feasible option, when the lattice thermal conductivity is much larger than the electronic one (that is, $\kappa_{ph} \gg \kappa_e$). In the past few decades, various approaches have been adopted, to improve the TE FOM (represented by $ZT = (\sigma \times S_B^2 \times T)/\kappa$, where σ, S_B, κ, and T are the electrical conductivity, Seebeck coefficient, total thermal conductivity ($\kappa_e + \kappa_{ph}$), and temperature value, respectively) greater than 1.[18,19] Though, it has always been a tough task to experimentally achieve a ZT value which is closer to or any greater than 1. What makes this optimization a challenging task is its individual components (e.g., S_B decreases with the increase in σ. Again, with the increase in σ, there will be a rise in κ_e value). Thus, having a very low value of κ_{ph} can be instrumental in improving the overall thermoelectric performance of any material.

For investigating the temperature dependent TE FOM of MoS_2, we have considered the monolayer flake having a length of 4.2 nm and a width of 1.6 nm (these values are consistent with the supercell dimensions of the previous studies[20–22]). Apart from the pristine nature, here in this study, we have also focused on the line defects, forming inversion domains (through which the monolayer changes its direction) in mechanically exfoliated MoS_2 samples. Such intrinsic line defects had been experimentally observed using transmission electron microscopy (TEM) (via, atomic resolution images) by Enyashin *et al.* in Ref. 20. Furthermore, Refs. 21 and 22 provide various analyses showing the effects of such line defects on electrical transport with the help of the density

[a]Electronic mail: dipsah_etc@yahoo.co.in
[b]Electronic mail: santanu@dese.iisc.ernet.in

functional tight binding (DFTB) method along with the non-equilibrium Green's function (NEGF) calculations. But, for a better understanding of the charge carrier transport as well as localization across the defect sites, we should rely on the density functional theory (DFT) which self-consistently obtains the electron density and in turn deduces the effective potential term of the Kohn-Sham equation. Thereby, in this paper, we have first studied different electronic properties of both the perfect and the defective samples using DFT. Utilizing the DFT-NEGF combination we have shown that, how the intrinsic carrier transport property of a monolayer MoS_2 flake gets hampered due to the existence of line defects. Later with the help of the parametrized Stillinger-Weber (SW) potential, we have demonstrated the lattice thermal conductance and phonon transmission through the samples. Finally, we have presented an analysis which depicts the temperature dependency of the TE FOM for the perfect as well as the defective monolayer MoS_2 flakes. We find that both the electrical as well as phonon transmission get hugely affected due to the presence of line defects. Moreover, at RT, the TE FOM for the monolayer MoS_2 has been obtained as ~0.2, which may not be as high as 1, but very much comparable with the values obtained for the other 2D materials like graphene[19] or, the one dimensional graphene nanoribbons.[23]

II. METHODOLOGY AND COMPUTATIONAL DETAILS

In this study, the density functional theory calculations are carried out using ATK (Atomistix Tool Kit).[24] The GGA-PBE (generalized gradient approximation along with the Perdew, Burke, and Ernzerhof functional) has been employed as the required exchange correlation.[25] Apart from that, the FHI (Fritz Haber Institute) pseudopotential used for the purpose of this work is a norm-conserving one.[26] The basis set that we have opted is DZP (double zeta polarized), which consists of three basis orbitals (the confined orbital, the one analytical split, and the polarization orbital for the first unoccupied shell of an atom) as implemented in ATK. The k-points in the Monkhorst-Pack grid are set to $1 \times 16 \times 16$. The monolayer MoS_2 (with the lattice constants of the hexagonal cell ~"a" = "b" = 3.16 Å) produces a bandgap ~1.69 eV (that is much closer to the experimental value compared with the DFTB obtained ~1.5 eV, as reported in the other study[21]). Besides, all the supercells are further relaxed until the maximum force tolerance value of 0.01 eV/Å is reached. The relaxed structures show a Mo-S bond length ~2.40 Å. For finding charge carrier redistribution, electron localization, and other intrinsic properties, we consider a 5×5 monolayer MoS_2 flake (as shown in Figs. 1(a)–1(c)). To avoid the spurious interactions between periodic images in "X" direction (along the thickness of the monolayer), we have incorporated a vacuum region of 20 Å. However, to obtain the electrical as well as thermal transport, we have converted those flakes (of Figs. 1(a)–1(c)) into the 2D sheets having dimensions 4.2 nm × 1.6 nm (as illustrated in Fig. 1(d)).

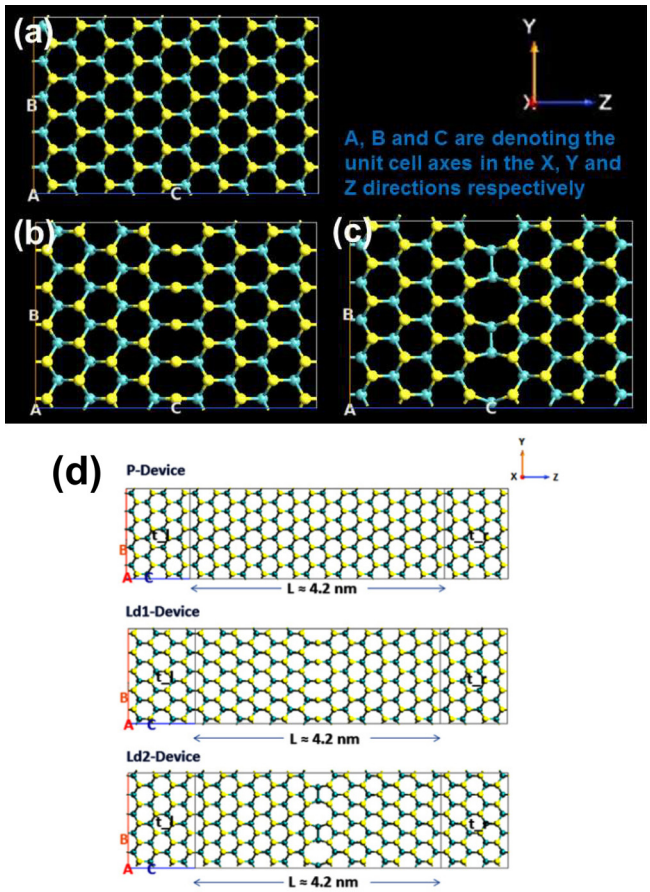

FIG. 1. (a) 5×5 monolayer MoS_2 flake without any defect; (b) with line defect having -s- bridges; and (c) Mo-Mo bonds. (d) The two-port device structures made of the perfect as well as the defective MoS_2 flakes.

III. RESULTS AND DISCUSSIONS

A. Effect of line defects on various electrical properties

Given the gigantic success of the mechanically exfoliated single layer graphene,[2] the same technique was also adopted to obtain the monolayers from the bulk transition-metal dichalcogenides (TMDs).[1,3,4] Alternatively, for the large-scale production of crystalline monolayer MoS_2, a different process called Chemical Vapor Deposition (CVD) is practised. But, it has been observed that the large-scale synthesis of CVD grown MoS_2 often ends up with a sample having lower carrier mobility.[27] The other possible suspects for such kind of performance degradation may be the various intrinsic structural defects, such as dislocations with 5–7 and 6–8 fold rings, point defects, grain boundaries, and line defects.[28,29] However, as mentioned earlier, in this study we have confined our study only to those line defects, which had already been experimentally observed in mechanically exfoliated MoS_2 samples.

In order to determine the electro-static difference potential (ΔV_H), the electron localization function (ELF), and the effect of spin polarization on density of states (DOS), we first considered a 5×5 monolayer MoS_2 flake where the periodicity is maintained in "Y" and "Z" directions (Fig. 1(a)). We then opted for the two most stable structures of MoS_2

flake with line defects as described in Ref. 20 (hereafter, these will be called as Ld1 and Ld2, if not otherwise mentioned). In Ref. 20, to estimate the most stable structure, Enyashin *et al*. developed atomistic models of MoS_2 layer fragments and then optimized using DFTB prior to performing a molecular dynamics (NVT ensemble; with temperatures 300 K and 600 K) simulations. According to their analysis, Ld1 (with -s- bridges, as shown in Fig. 1(b)) and Ld2 (with Mo-Mo bonds, as shown in Fig. 1(c)) are the two most stable configurations; which they further compared with the high resolution TEM images and found a very good match.

1. Electro-static difference potential

Although the effects of line defects on the electrical transport had previously been analysed to some extent in Ref. 22, but the study employed DFTB instead of DFT calculations with the CP2K basis set which inherently takes an approximation of frozen core. However, running a self-consistent iteration on top of that might have included some approximated atom-based electron density in to the picture and helped to find the necessary Hartree potential by relying on the redistribution of Mulliken charges.[30] Therefore, a more accurate and rigorous first-principles based DFT calculation in this regard is yet to be made. For the purpose, we have derived the electro-static difference potential (ΔV_H) for the perfect as well as Ld1 and Ld2 samples.

ΔV_H is generally meant for calculating the Hartree potential owing to a difference in density that actually takes place due to charge redistribution within the system. Comparing Fig. 2(b) with Fig. 2(a), we find that the ΔV_H is more positive around the site of the line defect (Ld1) with -s- bridges. This in turn relates to a higher difference density or charge accumulation near the region. Something similar happens in case of the other type of line defect (i.e., Ld2) also (Fig. 2(c)). But, here the maximum ΔV_H value is not consistent over the entire defect site, rather localized around the Mo-Mo bonds.

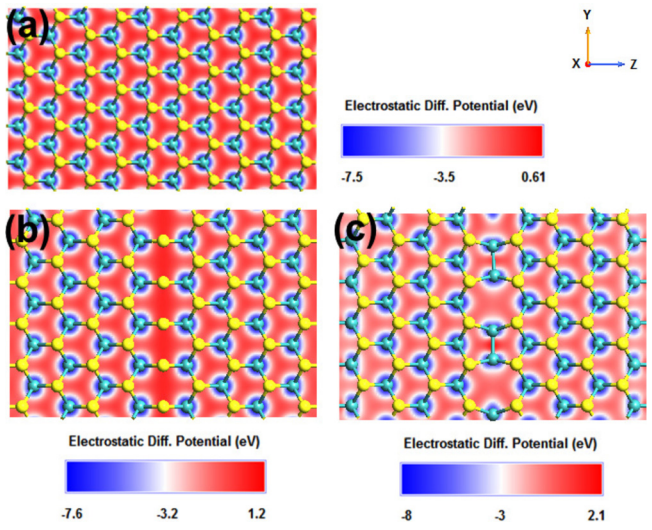

FIG. 2. Cut-plane images showing ΔV_H across "Y"-"Z" directions for (a) perfect MoS_2, (b) Ld1, and (c) Ld2 samples.

2. Electron localization

Electron localization function (ELF) is a measure of Pauli Repulsion which depends not only on the electron density and its gradient but also on the kinetic energy distribution.[31,32] The value of ELF lies between "0" and "1," where "1" denotes a region where electrons are greatly localized (thereby, it is almost unlikely that another electron with the same spin could be found in the vicinity of one).[32] On the other hand, any value close to "0" signifies the region between two electron shells.[32] However, ELF $\simeq$0.5 actually represents nothing but of the homogeneous electron gas.[31]

In Fig. 3, we show how the evenly distributed localization in the perfect monolayer changes, when there are line defects within the sample. With help of the colour map (ranges from "0" to "1"), we have compared the cut-plane images (across "Y"-"Z") for all the three samples (perfect, Ld1 and Ld2). Looking in to Figs. 3(b) and 3(c), we find that compared with the line defect site with -s- bridges in Ld1, the ELF is more localized around the Mo-Mo bonds of Ld2. This indicates higher probability of finding a covalent bond there. However, the blue spaces along the defect site with -s- bridges in Ld1 (Fig. 3(b)) clearly unveil the regions among the shells.

3. Effect of spin polarization on DOS

Figure 4 shows the density of states (DOS) diagram for the perfect as well as Ld1 and Ld2 samples. Owing to a previous study of Ref. 33 which shows sulfur-vacancy introduced magnetic moment in strain-manipulated monolayer MoS_2, here we have performed the spin polarization calculations to obtain DOS of various samples.

Considering the flakes Ld1 and Ld2, we observe that there are no significant differences between the up and down spin DOS-components of the individual defective samples. Moreover, the overall patterns (for, Ld1 and Ld2) of up and down spin DOS-components remain the same (although, there might be any local deviations seen). Therefore, while obtaining the results relating to ΔV_H, ELF, etc. (described in Subsections III A 1 and III A 2), we have actually considered the spin unpolarized calculations.

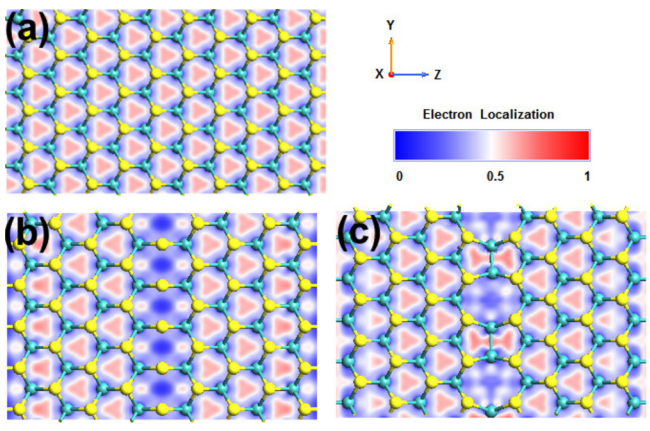

FIG. 3. Distribution of ELF across the plane for (a) 5 × 5 perfect monolayer MoS_2, as well as (b) Ld1, and (c) Ld2 flakes.

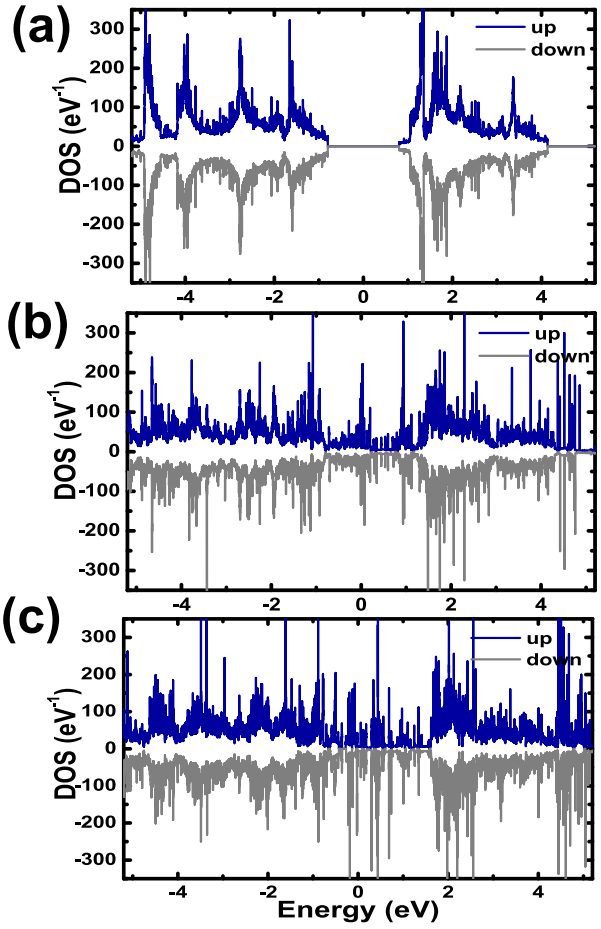

FIG. 4. Spin resolved DOS obtained for the 5×5 (a) perfect MoS_2 flake, (b) as well as the Ld1 sample, and (c) the Ld2 sample.

Further, to determine the electro-thermal transport behaviour of the perfect as well as the defective 2D sheets (in Section III B), we have calculated the various electrical parameters, e.g., conductance (G_e), thermal conductance due to charge carriers (K_e), Seebeck coefficient (S), etc., considering the "sum" of the up and the down spin components (obviously, for the spin unpolarized calculations, this "sum" is nothing but of 2 × up spin component or else, 2 × down spin component).

B. Electro-thermal transport and thermoelectric FOM

To determine electro-thermal transport properties of the perfect as well as defective 2D sheets, we altered the 5×5 flakes of Figs. 1(a)–1(c) into the larger samples of length (L) = 4.2 nm and width (W) = 1.6 nm and transformed those in to the two-port device structures (as shown in Fig. 1(d)). Here after, we will call the devices made of perfect, Ld1 and Ld2 defective samples as the P-device, the Ld1-device, and the Ld2-device, respectively. As illustrated in Fig. 1(d), t_l and t_r are the left and right electrodes (which are ~10.9 Å long). For device calculations, the k-points in the Monkhorst-Pack grid are taken as $1 \times 16 \times 99$. Figure 5 illustrates the device density of states (DDOS) diagrams, obtained at zero bias condition, for the three device structures (of Fig. 1(d)).

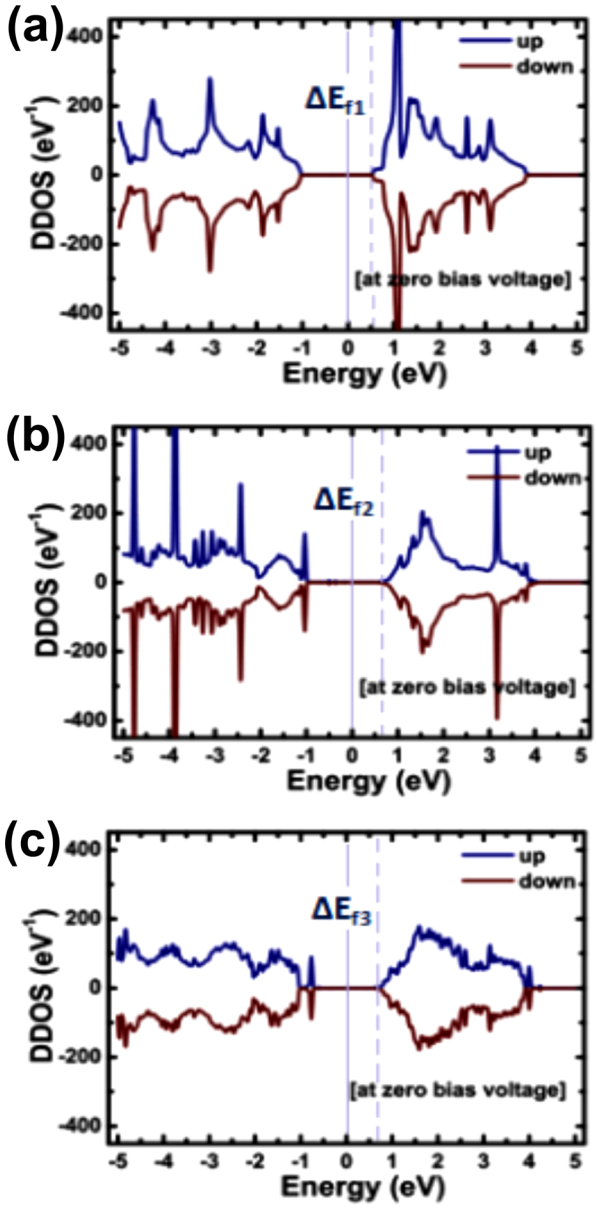

FIG. 5. The zero bias DDOS diagrams of the (a) P-device, (b) Ld1-device, and (c) Ld2-device, respectively. Because of spin unpolarized calculation, here the respective spin up and spin down components are simply the mirror images of each other.

Again, it is important to realize that for this entire study, the energy zero is represented as the position of the Fermi level (E_F). Thus, the energy axes of Figs. 4(a)–4(c), Fig. 5, as well as that of Figs. 6 and 7 and Fig. 8(a) are actually denoting the (E-E_F).

Now, considering the DDOS, we find that they display a significant difference in the overall nature, compared with their bulk forms (as shown earlier). Hence, the typical nature of the DDOS makes the role of the bias window extremely important in finding the electrical current for such ultra-small, narrow, and thin devices. As it was observed in the previous studies also,[21,22] the defect-borne states appear in the mid-gap region around (E_F) (which can be seen looking at Figs. 4(b) and 4(c)). But, it is interesting to note that those spurious states being strongly localized hardly contribute in the charge carrier transport (Fig. 6).[21] In Fig. 6, a comparison

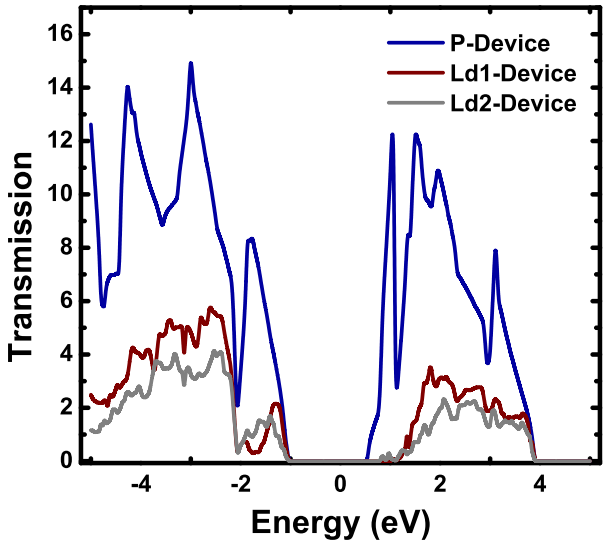

FIG. 6. Transmission spectrum of the P-device, the Ld1-device, and the Ld2-device for the entire range of −5 eV to 5 eV.

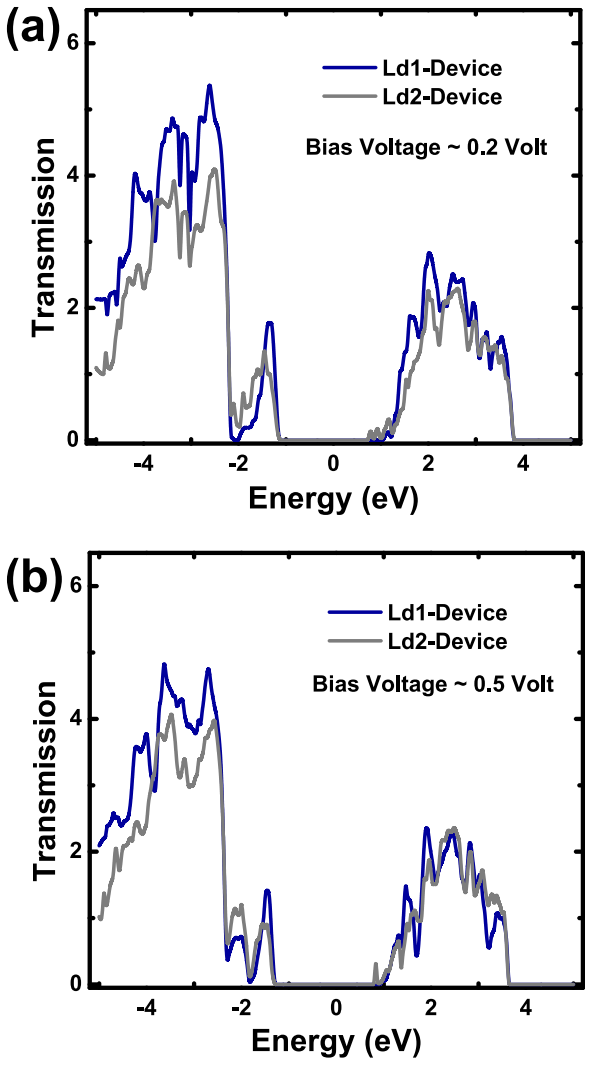

FIG. 7. Finite bias transmission of the devices with defective channels, for the bias voltage of (a) 0.2 V and (b) 0.5 V.

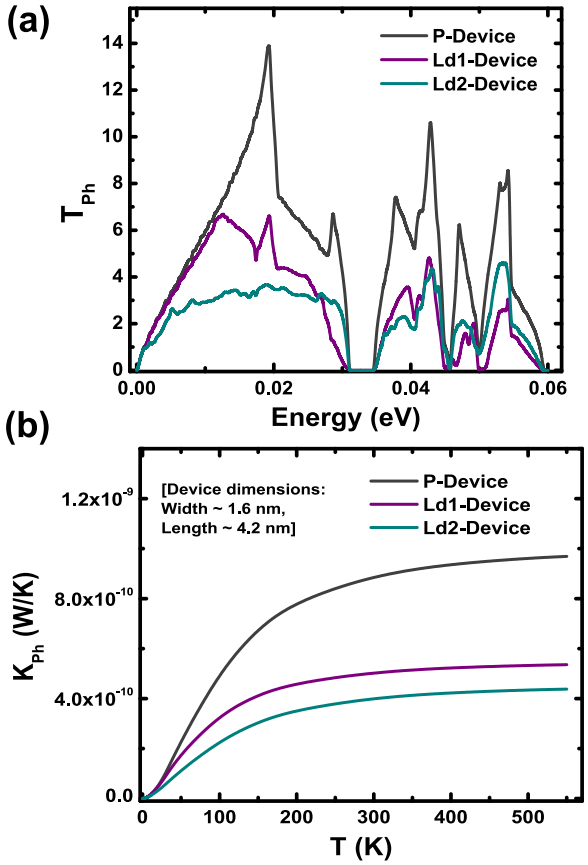

FIG. 8. (a) Phonon transmission spectra versus energy and (b) the corresponding temperature dependent lattice thermal conductance plots, taking all three device structures into account.

of the transmission spectrum (obtained at zero bias) of the P-device, the Ld1-device, and the Ld2-device has been illustrated. Taking the entire range of −5 eV–5 eV, we find that the transmission of charge carriers in Ld1-device is somewhat advantageous than that in the Ld2-device.

Moreover, looking in to the transmission spectra of the P-device, it can be seen that the forbidden region for any charge carrier transport around the energy zero is ∼1.6 eV, which is consistent with the bandgap as obtained for the 5×5 monolayer MoS_2 flake (illustrated in Fig. 4(a)). However, for P-device, the onset of electron transmission states takes place ∼0.55 eV. As seen in Fig. 6, this value is somewhat larger in case of the Ld1-device or, the Ld2-device. With reference to the energy zero, we find it as ∼0.95 eV for the Ld1-device and ∼0.75 eV for the Ld2-device. We denote these energy offsets as ΔE_{f1}, ΔE_{f2}, and ΔE_{f3} for the P-device, the Ld1-device, and the Ld2-device, respectively (Fig. 5). Next, we have considered two finite bias cases, one with the bias voltage of 0.2 V and the other one with 0.5 V (shown in Figs. 7(a) and 7(b)). Comparing the transmission spectra of the devices with defective channels, we find almost a similar trend that of the zero bias case. But, the impact of the defect-induced scattering becomes more and more as we increase the bias voltage.

However, as it was previously discussed, the phonon transmission is calculated using the parametrized SW (Stillinger-Weber) potential as depicted in Ref. 34 by Jiang

et al. In order to find the phonon transmission (via frozen phonon calculations), we need to form a dynamical matrix of the system, and for that we require a larger super cell which can effectively be perturbed. This imposes a major constraint for using DFT, as the calculation of the phonon related parameters for any large structure (e.g., the devices shown in Fig. 1(d), with a length of 4.2 nm and width of 1.6 nm) demands enormous computational resources. However, to overcome this barrier, we may take help of any well established classical potential which can quite accurately capture various experimentally observed phenomena. Among others, VFF (valance force field) is one of the interatomic potentials that had been successfully used for calculating the phonon dispersion curves of the bulk as well as the single layer MoS_2.[35,36] On the other hand, SW parametrized potential for monolayer MoS_2,[34] which has been obtained by calibrating the phonon dispersion curves along the Γ-M direction of the Brillouin zone, can provide a very good estimation of size and strain effects on Young's modulus, thermal conductivity, etc., Figure 8(a) portrays a comparison of phonon transmission spectra for the P-device, Ld1-device, and Ld2-device. We observe here no significant difference from the electrical counterpart as the phonon transmissions get heavily affected in both the defective samples (Ld1-device and Ld2-device). Here, also we find (at least, by analysing the contributions made by the acoustic modes) that the phonon transport gets more severely affected through the Ld2 channel compared with the Ld1. Furthermore, a clear gap around 31–34 meV (in energy axis) separates the contributions from the acoustic and the optical modes.

Figure 8(b) shows the characteristics of temperature dependent lattice thermal conductance (K_{ph}) for all the three device structures (based on the calculated T_{ph} as shown in Fig. 8(a)). Considering a quasi ballistic transport, the intrinsic phonon thermal conductance at RT for the P-device (with a $W \sim 1.6$ nm) has been computed as ≃0.894 nW/K (which is again consistent with the finding of Cai *et al*., as reported in Ref. 16). However, at the higher temperatures (>500 K), this value gets almost saturated around 0.97 nW/K. At RT, the lattice thermal conductance values for the Ld1-device and the Ld2-device have been obtained as ≃0.506 nW/K and ≃0.403 nW/K, respectively. Looking into those thermal conductance values for the entire temperature range of 0 K to 550 K, it can easily be seen that the line defects have a huge impact on the phonon thermal transport through any 2D MoS_2 channel.

Next, to explore the effect of line defects on the TE FOM, we have considered the three device structures of Fig. 1(d) and the corresponding electron and phonon transmission spectra as illustrated in Figs. 6 and 8(a). So far, we have analysed the results for all the three structures considering intrinsic behaviour. But for obtaining significant TE FOM, it is required to dope those samples either in to n-type or p-type. In this study, since we are interested in calculating *ZT* considering the n-type samples, hence we will shift the Fermi levels by the amounts ΔE_{f1}, ΔE_{f2}, and ΔE_{f3} for the P-device, the Ld1-device, and the Ld2-device, respectively. Moreover, to find out the TE FOM values for the perfect as well as defective samples, we can rewrite the expression of *ZT* as $ZT = (G_e \times S^2 \times T)/(K_e + K_{ph})$. The details and the derivations of G_e, K_e, S, and K_{ph} are available in Appendixes A and B. Typically, the dependence of S and K_e on the doping density depicts an opposite trend. Thereby, a combined metric $S^2 \times G_e$ (i.e., "power factor") can be much more useful for determining the thermoelectric behaviour. However, the term $(K_e + K_{ph})$ also plays a key role in predicting *ZT*; specially when the lattice part is much higher than the thermal conductance due to the charge carriers.

Figure 9 shows the variations of *ZT* for the P-device, the Ld1-device, and the Ld2-device, with the Fermi level shift (ΔE_f) at different temperatures. Considering the other reported calculation[37] and the measured values of sheet-concentration,[38] here in this study, we have restricted the Fermi level shift up to 1.15 eV (starting from 0.55 eV) only. We find that the maximum value of *ZT* for the P-device is around $\Delta E_f \sim 0.55$ eV. However, this trend is quite opposite in the case of Ld1-device structure. For the Ld1-device, we can see that the *ZT* increases as we increase ΔE_f and reaches a maximum value near $\Delta E_f \sim 1$ eV. Besides, for the Ld2-device, we observe a typical nature of the plot which indicates the maximum value of *ZT* around $\Delta E_f \sim 0.75$ eV. Hence, Fig. 9 apparently justifies the aforementioned values of the Fermi level shift (ΔE_{f1}, ΔE_{f2}, and ΔE_{f3}) for the three device structures.

The variation of TE power factor values with change in temperature has been shown in Fig. 10(a), whereas Fig. 10(b) describes the total thermal conductance ($(K_e + K_{ph})$) of the individual device structures as the function of temperature. For the purpose, we have varied the temperature over a long range (∼100 K–550 K).

Finally, the temperature dependence of *ZT* has been illustrated in Fig. 11. We find that for all the three device, *ZT* increases monotonically with temperature. However, at RT, the calculated TE FOM for the P-device is 0.195 which is consistent with the result (0.25 for n-type monolayer MoS_2) of Ref. 39 as reported by Huang *et al*. However, the *ZT* decreases quite significantly for the devices with defective flakes. At RT, TE FOM values for the Ld1-device and the Ld2-device are 0.0129 and 0.0704, respectively. Besides, for

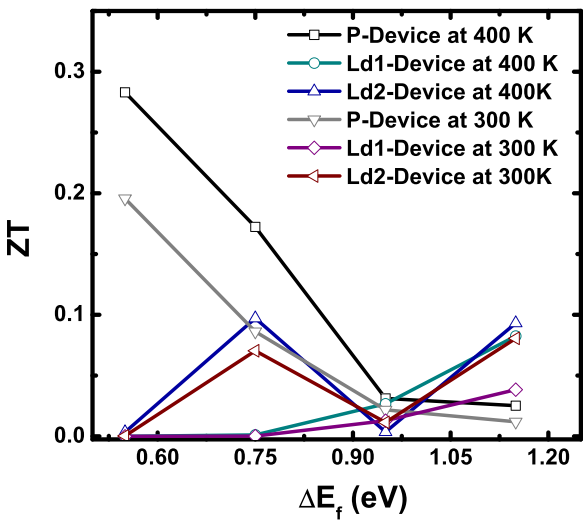

FIG. 9. Change in TE FOM with Fermi the level shift, for the P-device, the Ld1-device, and the Ld2-device.

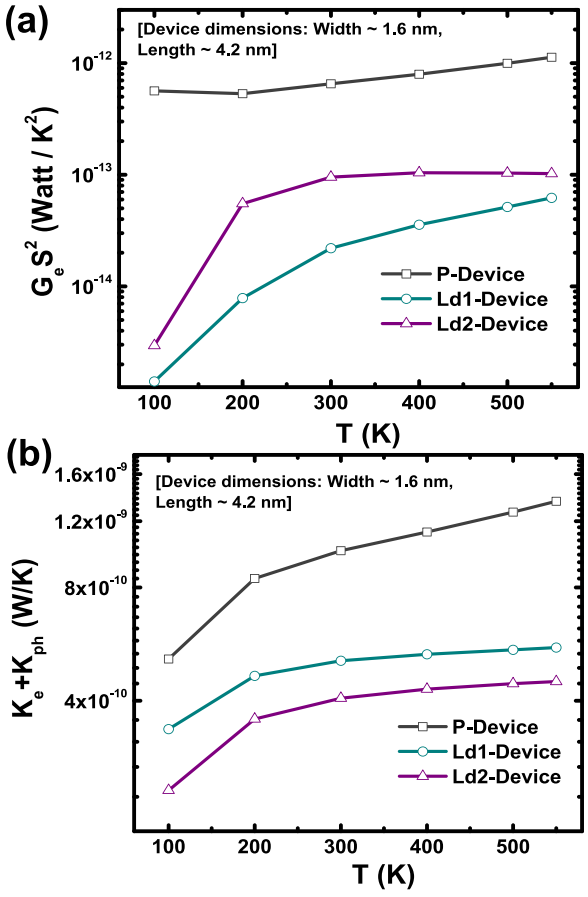

FIG. 10. (a) Plots of thermoelectric power factor and (b) the total thermal conductances ($(K_e + K_{ph})$) for the P-device, the Ld1-device, and the Ld2-device, over a temperature range of 100 K to 550 K. The Y-axes are plotted in logarithmic-scale, for the better description of the sharp changes which take place near 100 K.

any higher temperature, e.g., 500 K, the *ZT* values for the P-device, the Ld1-device, and the Ld2-device are obtained as 0.392, 0.047, and 0.116, respectively.

From Fig. 11, it can easily be inferred that the TE FOM of monolayer MoS_2 gets severely affected by the presence of

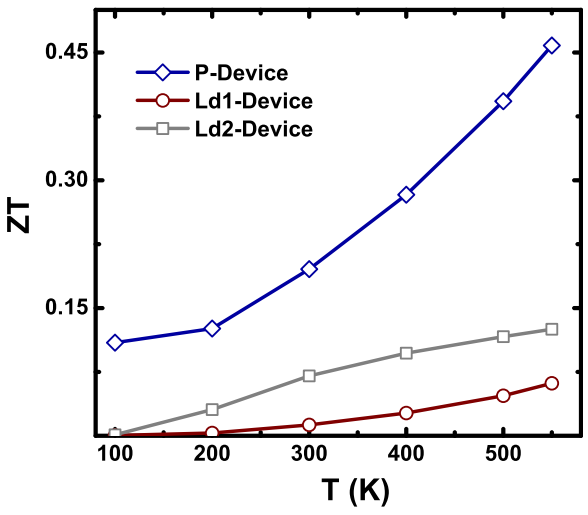

FIG. 11. ZT versus temperature for all the three device structures. Temperature is varied within the range of ~100 K to 550 K.

intrinsic line defects. Moreover, considering the *ZT* values over the entire temperature range (100 K–550 K), we find that the TE FOM gets more affected by the line defect Ld1 compared with Ld2.

IV. CONCLUSION

Here, in this work, we have tried to establish the impact of line defects on the charge carrier transport as well as lattice thermal transport of the monolayer MoS_2. First, with help of the first-principles based DFT calculations, we have shown how the various important electronic properties, e.g., electro-static difference potential, ELF, etc., vary for the different line defective samples (Ld1, Ld2). Next, we have determined the transmission through the perfect and the defective samples and found that the transmission of the charge carriers sees a considerable amount of reduction, when there is a line defect situated inside the flake. Furthermore, it has been observed that the transmission of charge carriers in the Ld1-device is somewhat more advantageous than that in the Ld2-device. A very similar trend can be found for the lattice thermal transport also. The thermal conductance due to lattice vibrations (at 300 K) for the perfect monolayer MoS_2 is $\simeq$0.894 nW/K. But, this gets deteriorated to $\simeq$0.506 nW/K for the device with Ld1 channel and $\simeq$0.403 nW/K for the device with Ld2 channel.

However, looking into the TE FOM obtained at RT, we can find that the n-type MoS_2 channel with line defect Ld2 produces better results compared to the same with line defect Ld1. But, importantly it has been evinced that the overall electro-thermal transport in a mechanically exfoliated monolayer MoS_2 flake can greatly be tuned by considering the two stable configurations of line defects with -s- bridges or Mo-Mo bonds.

ACKNOWLEDGMENTS

This work was supported by the Department of Science and Technology, Government of India, under Grant No. SR/S3/EECE/0151/2012. Authors would also like to thank Dr. Troels Markussen, Dr. Anders Blom, and Dr. Julian Schneider of QuantumWise A/S Copenhagen, Denmark, for the useful discussions.

APPENDIX A: CALCULATIONS OF CHARGE CARRIER TRANSPORT

For the purpose of deriving the electrical transport along the length of the channel, we employed the NEGF method along with the DFT calculations. One of the key assumptions there was that the systems were in steady sate.[40] Besides, the self-consistent Hartree potential of both the right and the left electrodes was determined first. Then, the same for the central region had been obtained by solving the Poisson's equation.[40,41] Moreover, for obtaining the transmission spectra, we had used the "Recursion-Self Energy" calculator and set the position of the Fermi level (E_F) to the energy zero.

Now, using the NEGF formalism, the electronic transmission through the channel can be found as

$$T_e(E) = \mathrm{Tr}[\Gamma_l(E)\, G(E)\, \Gamma_r(E)\, G^{\dagger}(E)], \tag{A1}$$

where $G(E) = [EI - H' - \Sigma_l(E) - \Sigma_r(E)]$ and $G^{\dagger}(E)$ represents the retarded Green's function and the advanced Green's function, respectively. H' represents the Hamiltonian of the channel, and I denotes the identity matrix.[41,42] Apart from that the $\Gamma_{l,r}(E) = i[\Sigma_{l,r} - \Sigma_{l,r}^{\dagger}]$ are the broadening matrices (formed by setting up the self energy matrices Σ_l and Σ_r) for the left and the right electrodes.[42] Now, with help of the Landauer-Büttiker formalism,[43,44] the electrical current can be obtained as

$$I = \frac{2q}{h} \int_{-\infty}^{+\infty} T_e(E)\, \left[f(E,\mu_l) - f(E,\mu_r)\right] dE, \tag{A2}$$

where h is the Planck's constant. q denotes the charge of an electron, and T_e represents transmission function per spin (considering "up" or "down") obtained using the self-consistent DFT-NEGF combination. $f(E, \mu)$ is the Fermi distribution function. Other than that, the bias voltage between the end terminals is related to the chemical potentials as, $(\mu_l - \mu_r) = \mathrm{V} \times \mathrm{q}$.[43]

Thus, the electrical conductance due to the charge carriers can be formulated as[42]

$$G_e(\mu) = \frac{2q^2}{h} \int_{-\infty}^{+\infty} T_e(E) \left(\frac{-\partial f(\mu,E)}{\partial E}\right) dE. \tag{A3}$$

Utilizing the concept of linear coherent transport, in the near equilibrium region, the above equation can be rewritten as[44]

$$G_e(\mu) = q^2 \times L_{f,0}, \tag{A4}$$

where the general form of the function $L_{f,n}(\mu)$ is[42,44] $L_{f,n}(\mu) = \frac{2}{h} \times \int_{-\infty}^{+\infty} T_e(E)\, (E-\mu)^n \left(\frac{-\partial f(\mu,E)}{\partial E}\right) dE$.

Beside, under the linear response approximation, the thermal conductance due to the charge carriers and the Seebeck co-efficient (which depicts the induced thermoelectric voltage due to the change in temperature) can be expressed as[44,45]

$$K_e = \frac{1}{T} \times \left(L_{f,2} - \frac{L_{f,1}^2}{L_{f,0}}\right), \tag{A5}$$

and

$$S = \frac{1}{qT} \times \frac{L_{f,1}}{L_{f,0}}. \tag{A6}$$

APPENDIX B: CALCULATIONS OF PHONON TRANSPORT

For calculating the phonon transmission via NEGF, the same formalism (as it had been employed for the case of electrical transmission) was followed. There, we made the following substitutions: $EI \rightarrow \omega^2 M_a$ and $H' \rightarrow K'_{ch}$.[42,45] Moreover, for quasi ballistic transport at RT (as, the anharmonic phonon-phonon interaction part was not considered), the phonons of all energies did contribute to the total thermal conductance.[46]

In the aforementioned substitutions, ω denotes the frequency, and M_a illustrates the diagonal matrix having elements representing the mass of the atoms. K'_{ch} is describing the dynamical matrix of the channel region. Similarly, for the electrodes, the self energy matrices $(\Sigma_{l,r})$ can be found as the function of ω.[42] The phonon thermal conductance (with help of the phonon transmission co-efficient T_{ph}, which is again the function of ω) can be found as[45,46]

$$K_{ph}(T) = \frac{1}{2\pi} \int_0^{\infty} \hbar\omega\, T_{ph}(\omega) \times \left(\frac{\partial n(\omega,T)}{\partial T}\right) d\omega, \tag{B1}$$

where $n(\omega,T)\,(= (e^{\hbar\omega/k_BT} - 1)^{-1})$ is the Bose-Einstein distribution at average temperature T, and k_B denotes the Boltzmann constant. Considering linear response, for any small temperature variation (δT) between the two electrodes (such that $T_{t\_l} = T + (\delta T/2)$ and $T_{t\_r} = T - (\delta T/2)$), we can replace the $\frac{\partial n(\omega,T)}{\partial T}$ with $\frac{\hbar\omega}{k_BT^2} \times \frac{e^{\hbar\omega/k_BT}}{(e^{\hbar\omega/k_BT}-1)^2}$. Thus, Eq. (B1) can be rewritten as[42]

$$K_{ph}(T) = \frac{\hbar^2}{2\pi k_B T^2} \int_0^{\infty} \omega^2 T_{ph}(\omega) \times \frac{e^{\hbar\omega/k_BT}}{\left(e^{\hbar\omega/k_BT} - 1\right)^2} d\omega. \tag{B2}$$

[1] B. Radisavljevic, A. Radenovic, J. Brivio, V. Giacometti, and A. Kis, Nat. Nanotechnol. **6**, 147–150 (2011).
[2] K. S. Novoselov *et al.*, Proc. Natl. Acad. Sci. U. S. A. **102**(30), 10451–10453 (2005).
[3] K. F. Mak, C. Lee, J. Hone, J. Shan, and T. F. Heinz, Phys. Rev. Lett. **105**, 136805 (2010).
[4] D. Lembke and A. Kis, ACS Nano **6**, 10070–10075 (2012).
[5] S. Bhattacharya, D. Saha, A. Bid, and S. Mahapatra, IEEE Trans. Electron Devices **61**, 3646–3653 (2014).
[6] C. D. English, G. Shine, V. E. Dorgan, K. C. Saraswat, and E. Pop, "Improving contact resistance in MoS_2 field effect transistors," in *72nd Annual Device Research Conference* (2014), pp. 193–194.
[7] S. Das, H.-Y. Chen, A. V. Penumatcha, and J. Appenzeller, Nano Lett. **13**, 100–105 (2013).
[8] S. Bertolazzi, J. Brivio, and A. Kis, ACS Nano **5**, 9703–9709 (2011).
[9] A. A. Balandin, Nat. Mater. **10**, 569–581 (2011).
[10] K. I. Bolotin *et al.*, Solid State Commun. **146**, 351–355 (2008).
[11] R. Verma, S. Bhattacharya, and S. Mahapatra, Semicond. Sci. Technol. **28**(1), 015009 (2013).
[12] T. P. Kaloni *et al.*, Europhys. Lett. **98**, 67003 (2012).
[13] T. P. Kaloni *et al.*, Chem. Phys. Lett. **534**, 29–33 (2012).
[14] J. Xue *et al.*, Nat. Mater. **10**, 282–285 (2011).
[15] R. Yan, J. R. Simpson, S. Bertolazzi, J. Brivio, M. Watson, X. Wu, A. Kis, T. Luo, A. R. Hight Walker, and H. G. Xing, ACS Nano **8**, 986 (2014).
[16] Y. Cai, J. Lan, G. Zhang, and Y.-W. Zhang, Phys. Rev. B **89**, 035438 (2014).
[17] D. Saha and S. Mahapatra, "Analytical insight into the lattice thermal conductivity and heat capacity of monolayer MoS_2," Physica E (in press).
[18] L. D. Hicks and M. S. Dresselhaus, Phys. Rev. B **47**, 12727–12731 (1993).
[19] R. Verma, S. Bhattacharya, and S. Mahapatra, IEEE Trans. Electron Devices **60**(6), 2064–2070 (2013).
[20] A. N. Enyashin, M. Bar-Sadan, L. Houben, and G. Seifert, J. Phys. Chem. C **117**, 10842–10848 (2013).
[21] M. Ghorbani-Asl, A. N. Enyashin, A. Kuc, G. Seifert, and T. Heine, Phys. Rev. B **88**, 245440 (2013).
[22] A. Sengupta, D. Saha, T. A. Niehaus, and S. Mahapatra, IEEE Trans. Nanotechnol. **14**, 51–56 (2015).

[23]W. Huang, J.-S. Wang, and G. Liang, Phys. Rev. B **84**, 045410 (2011).
[24]See http://quantumwise.com/ for QuantumWise Atomistic ToolKit (ATK) with Virtual NanoLab.
[25]J. P. Perdew, K. Burke, and M. Ernzerhof, Phys. Rev. Lett. **77**(18), 3865 (1996).
[26]See http://www.quantum-espresso.org/pseudo-search-results/ for Pseudo Search Results.
[27]K.-K. Liu *et al*., Nano Lett. **12**, 1538–1544 (2012).
[28]W. Zhou *et al*., Nano Lett. **13**, 2615–2622 (2013).
[29]X. Zou, Y. Liu, and B. I. Yakobson, Nano Lett. **13**, 253–258 (2013).
[30]M. Elstner *et al*., Phys. Rev. B **58**, 7260–7268 (1998).
[31]A. D. Becke and K. E. Edgecombe, J. Chem. Phys. **92**, 5397–5403 (1990).
[32]A. Savin *et al*., Angew. Chem., Int. Ed. Engl. **31**(2), 187–188 (1992).
[33]W. S. Yun and J. D. Lee, J. Phys. Chem. C **119**, 2822–2827 (2015).
[34]J.-W. Jiang, H. S. Park, and T. Rabczuk, J. Appl. Phys. **114**, 064307 (2013).
[35]N. Wakabayashi, H. G. Smith, and R. M. Nicklow, Phys. Rev. B **12**, 659–663 (1975).
[36]S. J. Sandoval, D. Yang, R. F. Frindt, and J. C. Irwin, Phys. Rev. B **44**(8), 3955–3962 (1991).
[37]T. Gunst *et al*., "Mobility and bulk electron-phonon interaction in two-dimensional materials," in *International Conference on Simulation of Semiconductor Processes and Devices (SISPAD)* (2015), pp. 32–35.
[38]B. Radisavljevic and A. Kis, Nat. Mater. **12**, 815–820 (2013).
[39]W. Huang, H. Da, and G. Liang, J. Appl. Phys. **113**, 104304 (2013).
[40]The NEGF formalism in ATK, see http://www.quantumwise.com/documents/manuals/latest/ReferenceManual/.
[41]M. Brandbyge *et al*., Phys. Rev. B **65**, 165401 (2002).
[42]T. Markussen, A.-P. Jauho, and M. Brandbyge, Phys. Rev. B **79**, 035415 (2009).
[43]M. Büttiker *et al*., Phys. Rev. B **31**, 6207–6215 (1985).
[44]K. Esfarjani, M. Zebarjadi, and Y. Kawazoe, Phys. Rev. B **73**, 085406 (2006).
[45]J.-W. Jiang, J.-S. Wang, and B. Li, J. Appl. Phys. **109**, 014326 (2011).
[46]H. Karamitaheri, M. Pourfath, H. Kosina, and N. Neophytou, Phys. Rev. B **91**, 165410 (2015).